Check for updates

Au–Ag controllable composition nanoalloying of hexagonal nanoplates: heterogeneous interfacial nanogaps enhance near-field focusing†

Sungbeen Park,[a] Insub Jung,[a] Soohyun Lee,[b] Qiang Zhao,[b] Sungwoo Lee,[b,c]
Hyunji Kim[a] and Sungho Park ⬚ *[a]

In this study, we present a novel strategy for fabricating binary-array surface-enhanced Raman scattering (SERS) substrates composed of gold (Au) and silver (Ag) plasmonic hexagonal nanoplates (h-NPLs), functioning as a "nanoalloy" system. Using Au h-NPLs as scaffolds, we synthesized Ag h-NPLs of closely identical sizes and shapes, facilitating the construction of a mixed plasmonic system. The flat morphology of h-NPLs enables their face-to-face assembly into parallel "wire-like string" arrays, referred to as "columnar superpowders (SPs)", which expose nanogaps perpendicular to the incident light and maximize near-field focusing. We achieved anisotropic superstructures of Au–Ag core–shell h-NPLs through epitaxial Ag growth on Au surfaces, controlled by the interplay of halide ions and surface crystal energy differences. Free-standing columnar SPs were fabricated *via* an upside-down assembly method, forming dense face-to-face nanogaps that act as hotspots for SERS enhancement. The thickness of the Ag shell was critical in optimizing plasmonic coupling between the Au core and Ag shell, thereby enhancing near-field effects. The observed strong near-field focusing originates from synergistic intra- and inter-interface plasmonic coupling, which induces a mirror charge effect, amplifying near-field polarization and SERS sensitivity. Theoretical simulations and experimental bulk SERS analyses validated these effects, underscoring the potential of binary-component nanoalloy structures for advanced optical sensing technologies. This work highlights the critical role of heterogeneous interfacial nanogaps in enhancing both near- and far-field plasmonic effects, paving the way for next-generation SERS applications.

Introduction

Traditionally, alloys are produced through atomic mixing, which enhances the properties of constituent metals, such as improved corrosion resistance and mechanical strength. In the synthesis of plasmonic nanoparticles (NPs), a similar atomic mixing approach has been widely employed, particularly for NPs composed of gold (Au), silver (Ag), and copper (Cu), which exhibit notable plasmonic behavior in the visible and near-infrared regions.[1,2] By adjusting the ratios of these components during atomic mixing, the localized surface plasmon resonance (LSPR) peak can be fine-tuned, achieving character-istics intermediate between those of the individual pure NPs.[3,4]

While combining different metals offers the potential to enhance and balance their individual plasmonic properties, a significant challenge arises in understanding the plasmonic effects when two identical NPs, differing only in their outer compositions, are mixed at the nanoscale. Distinct from atomic mixing, "nanoscale alloying" involves mixing NPs with identical shapes and sizes but differing outer compositions. This approach achieves long-range ordering in the assembly structure, allowing bulk properties to be consistently tailored by simply varying the ratios of the individual building blocks. As an exemplary application, the enhancement of surface-enhanced Raman spectroscopy (SERS) using nanoalloy-based SERS substrates is particularly compelling.[5] Most research on bulk SERS substrates has focused on single-component, monodisperse plasmonic building blocks.[6] The design of binary nanoalloy assemblies offers an exciting opportunity to advance SERS performance by leveraging the synergistic properties of mixed-component systems.

[a] Department of Chemistry, Yonsei University, Seoul 03722, Republic of Korea. E-mail: sparknano@yonsei.ac.kr
[b] Department of Chemistry, Sungkyunkwan University (SKKU), Suwon 16419, Republic of Korea
[c] Institute of Basic Science, Sungkyunkwan University (SKKU), Suwon 16419, Republic of Korea
† Electronic supplementary information (ESI) available. See DOI: https://doi.org/10.1039/d5nr01140j

Among various types of NPs, nanoplates (NPLs) are particularly unique anisotropic structures with distinct optical properties. They support multiple resonant plasmonic modes, including in-plane and out-of-plane modes, and exhibit tunable optical properties spanning from the visible to near-infrared (NIR) spectral regions, along with a large spatial surface area.[7,8] While the synthesis of Au NPLs is well-established,[9–11] achieving precise control over the shape and ensuring uniformity in size and morphology of Ag NPLs remains a significant challenge. This limitation hampers the full utilization and exploration of Ag NPLs' unique properties despite Ag's strong plasmonic characteristics, attributed to its high-quality factor.[12–14] In particular, hexagonal NPLs (h-NPLs) exhibit well-defined sharp edges and corners that localize plasmonic fields more effectively, thereby enhancing Raman signal amplification. However, the synthesis of highly homogeneous Ag h-NPLs has been scarcely reported due to the intrinsic chemical instability of Ag.[15] Strategies such as light-induced synthesis and polyvinylpyrrolidone (PVP)-mediated methods have been employed to produce Ag NPLs, revealing important insights into photochemical reactions and Ag reduction mechanisms.[16–18] However, achieving uniformity in size and shape during solution-phase synthesis remains challenging. This uniformity is crucial for particle assembly, as precise shape and size matching of individual building blocks is key to achieving well-organized and stacked self-assemblies, which enhance inter-particle plasmonic coupling in SERS.[19,20] Moreover, investigating near-field and far-field plasmonic coupling in heterogeneous and binary plasmonic building blocks, such as those combining Au and Ag, introduces additional complexity. Reports have been limited to core–shell NPs[21,22] or dimeric configurations of Au and Ag NPs,[23–27] which highlight the critical role of heterogeneous interfaces in influencing light–matter interactions.

Here, we report the fabrication of nano-alloyed Au–Ag h-NPLs using binary constituents of pure Au h-NPLs and Au@Ag h-NPLs. To synthesize Au–Ag core–shell h-NPLs, Au h-NPLs were employed as core templates, providing structural durability and chemical stability, while the outer Ag hexagonal shells retained the intense plasmonic properties of Ag. Leveraging the crystal facet energy differences between {111} and {100} planes of Au h-NPLs, well-controlled epitaxial growth of Ag on the Au cores was achieved, allowing the resulting structures to maintain their hexagonal geometry with tunable Ag shell thickness. The unique geometry of the h-NPLs, characterized by large top and bottom basal planes relative to the side height, enabled face-to-face "wire-like string" self-assembly under controlled depletion forces between the building blocks and surfactant micelles. This process led to the formation of columnar superpowders (SPs) —ready-to-use, free-standing supercrystals containing a high density of face-to-face nanogaps exposed to incoming laser light, thereby maximizing SERS activity. By assembling Au@Ag core–shell h-NPLs in close proximity, enhanced near-field collection was achieved through synergistic effects of intra-bimetallic interactions and inter-particle plasmonic coupling.

The role of Ag shell thickness in modulating intra-bimetallic effects and enhancing near-field collection was elucidated. Importantly, we synthesized binary nanoalloys composed of two distinct building blocks with similar dimensions: pure Au h-NPLs and Au@Ag h-NPLs with tunable volume ratios. This approach induced a mirror charge effect within the inter-particle nanogaps. Unlike conventional atomic alloy mixtures, this "nanoalloying" strategy relies on combining two distinct surface compositions at the nanoscale. The differing Au and Ag surfaces created imbalanced polarization degrees at the heterogeneous interfaces, significantly amplifying the near-field enhancement within the metallic nanogaps. Using this strategy, we achieved maximized SERS enhancement compared to SPs composed solely of pure Au or Au@Ag h-NPLs.

Experimental

Instrumentation

Field-emission scanning electron microscopy (FE-SEM) images were obtained using JSM-7610F-Plus, JSM-IT-500HR instruments (JEOL) and SU-5000 (Hitachi). Transmission electron microscopy (TEM) analysis was performed using JEM-F200 instruments (JEOL). UV–vis–NIR absorption spectra were acquired with a Shimadzu UV-3600 spectrophotometer. Raman spectra were measured using an XperRAM-S700 Raman microscope (Nanobase).

Chemicals

Hydrogen tetrachloroaurate(III) hydrate (HAuCl$_4$·nH$_2$O, 99%) was purchased from Kojima. Silver nitrate (AgNO$_3$, 99.8%) and sodium borohydride (NaBH$_4$, 98.0%) were obtained from Junsei. Sodium iodide (NaI, 99.5%), L-ascorbic acid (C$_6$H$_8$O$_6$, 99.5%), sodium hydroxide (NaOH, 97%), and trisodium citrate dihydrate were sourced from Sigma Aldrich Hexadecyltrimethylammonium bromide (CTAB, C$_{19}$H$_{42}$BrN, 99%) was obtained from Acros Organics, while hexadecyltri-methylammonium chloride (CTAC, C$_{19}$H$_{42}$ClN, 95.0%) was procured from Tokyo Chemical Industry, Japan. All chemicals were dissolved in triply distilled water (≥18.2 MΩ cm) prepared using a Milli-Q water purification system (Millipore).

Synthesis of Au hexagonal nanoplates (h-NPLs)

The synthesis of Au triangular nanoplates followed the methodology outlined in previous literature.[28] First, 10 mL of 0.05 M aqueous CTAB solution and 250 μL of 20 mM HAuCl$_4$ were added to 10 mL of the Au triangular nanoplate solution. The triangular nanoplates were etched with gold ions at 50 °C for 2 h, resulting in circular Au nanoplates. Residual Au ions were removed by centrifugation at 8000 rpm for 10 min, repeated twice. To synthesize Au hexagonal nanoplates, 10 mL of 0.1 M aqueous CTAB solution was mixed with 200 μL of 20 mM HAuCl$_4$, 200 μL of 100 mM ascorbic acid, and 5 mL of the Au circular nanoplate solution. After 1 h, the CTAB surfactant was removed by centrifugation at 6000 rpm for 10 min, repeated twice.

Synthesis of Au@Ag h-NPLs

Au@Ag h-NPLs were synthesized by overgrowing Ag on Au h-NPLs in the presence of a CTAC surfactant, with $AgNO_3$ acting as the Ag precursor. A solution was prepared by adding 40 mL of 0.1 M aqueous CTAC, 100, 200, or 300 μL of 2 mM $AgNO_3$, 100, 200, or 300 μL of 10 mM ascorbic acid, and 100, 200, or 300 μL of 0.1 M NaOH to 5 mL of Au h-NPLs. After 30 min, additional 2 mM $AgNO_3$ and 10 mM ascorbic acid were introduced into the reaction mixture, followed by another 30 min of incubation. The CTAC surfactant was then removed by two rounds of centrifugation at 8000 rpm for 10 min each. Finally, the resulting NPs were dispersed in water.

Forming the superpowders (SPs)

To form SPs, 1 mL of the NP solution was concentrated to 100 μL by centrifugation at 8000 rpm for 3 min. Subsequently, 1 mL of 2 mM CTAC solution was added to the concentrated solution, which was further concentrated to 40 μL by another round of centrifugation at 8000 rpm for 3 min. A total of 12 droplets (≈36 μL, with 3 μL per droplet) of the colloidal solution were drop-cast onto a silicon wafer. The wafer, containing sessile droplets, was inverted in a pressure- and humidity-controlled chamber. The inverted Si wafer with NPs was placed in a high-pressure chamber (4 bar) filled with N_2 gas (purity >99.99%) and incubated in a 30 °C oven for 12 h, resulting in well-formed superstructures on the Si wafers. The substrates were then immersed in ethanol for 5 min to remove organic compounds, including CTAC. After immersion, they were air-dried at room temperature. Finally, the superstructures were gently detached from the substrates using clean tweezers and stored in a vial at 4 °C.

Experimental conditions for SP SERS measurements

SERS substrates, including SPs of Au h-NPLs, Au@Ag h-NPLs, and Au–Ag binary h-NPLs, were prepared and saturated in 10^{-2} M 2-naphthalenethiol (2-NTT) dissolved in absolute ethanol at room temperature for 3 h. After saturation, the substrates were washed in absolute ethanol for 10 min. SERS measurements were conducted using a 785 nm excitation laser with a power of 780 μW. A microscope equipped with a 20× objective lens (NA = 0.34) and a charge-coupled device (CCD) detector was used to focus the laser onto the substrate surface. Measurements utilized large-area mapping (50 × 50 μm^2) with a 5 μm interval, a 1 s exposure time per mapping pixel, and a spectral range of 0 to 2000 cm^{-1}.

Electric field simulation

Electromagnetic simulations, including calculations of electric field enhancements, theoretical extinction cross sections, and surface-charge distributions of NPs, were performed using the finite element method (FEM) in commercially available software (COMSOL Multiphysics 6.0) with the RF module and frequency domain study. Models were constructed using AutoCAD software based on transmission electron microscopy (TEM) and scanning electron microscopy (SEM) data. In the

assembly simulations, the gap between NPs was set to 5 nm. The maximum tetrahedral mesh size for the simulation region in single-particle and assembly simulations was 10 nm, with a minimum size of 0.1 nm. The refractive index of the surrounding medium was set to that of water, as reported by Hale and Querry, while the refractive index of gold was defined using the empirical dielectric function provided by Johnson and Christy.

Detection of pesticide using SPs

Thiram solutions of varying concentrations were prepared for SERS measurements using SPs of Au, Au@Ag, and Au–Ag binary h-NPLs. Apple peels were washed with DIW and ethanol to remove organic contaminants. Next, 10 μL of Thiram solutions were applied to the apple peels and air-dried at room temperature. After drying, optical patches containing SPs were placed on the peel surface and incubated at room temperature for 5 min to achieve complete Thiram saturation on the SPs. SERS measurements were conducted using a 785 nm laser (4.0 mW) and a microscope equipped with a 20× objective lens (NA = 0.34) with an integration time of 1 s. Measurements employed large-area mapping (50 × 50 μm^2) with a 5 μm interval.

Results and discussion

Nanoalloying of SPs composed of Au h-NPLs and Au@Ag h-NPLs

In this study, we hypothesize that Au@Ag h-NPLs can generate strong near-field enhancement through both intra- and inter-particle plasmonic coupling, surpassing the near-field effects of their pure Ag or Au counterparts. When Au and Au core-Ag shell NPLs are assembled into a parallel string superstructure, two types of enhancements occur: (1) the intra-bimetallic interface effect within the core–shell structured Au@Ag h-NPLs and (2) the inter-mirror charge effect between neighboring Au and Au@Ag shell h-NPLs, as schematically illustrated in Fig. 1. The mirror charge effect refers to the increased polarization at heterogeneous interfaces due to imbalanced electron affinities between two distinct elements, leading to enhanced near-field effects.[19] This enhancement becomes even more pronounced when combining two different configurations, such as Au@Ag and pure Au h-NPLs, resulting in an anomalous mirror charge effect created by interfacial interactions between the two. We term this heterogeneous near-field enhancement, arising from the combination of distinct interfaces, the "asymmetric mirror charge effect".

Synthesis of Au@Ag h-NPLs

The Au@Ag core–shell h-NPLs were synthesized by first preparing Au h-NPLs as core templates using a seed-mediated method. The initial formation of these NPLs involved transforming Au triangular NPLs into regular h-NPLs with stereographic edges.[8] In this process, triangular Au NPLs with an edge length of 163 ± 13 nm (Fig. 2A) were converted into circu-
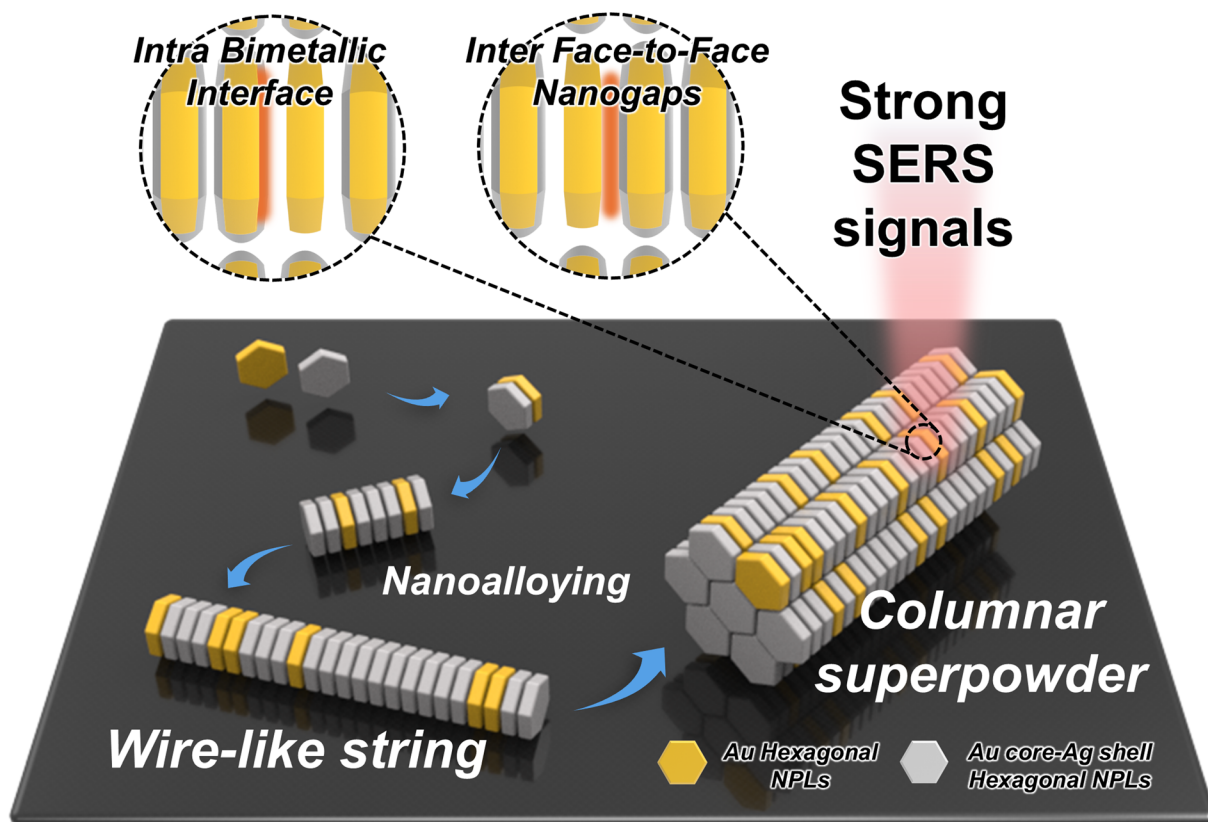
Fig. 1 Schematic illustration of the nanoalloying process used to create columnar SPs composed of pure Au h-NPLs and Au@Ag h-NPLs. Two types of plasmonic couplings contribute to near-field enhancement: (1) intra-plasmon coupling at the bimetallic interfaces within Au@Ag h-NPLs and (2) inter-plasmonic coupling through face-to-face nanogaps between heterogeneous Au and Au@Ag interfaces. This nanoalloying induces an asymmetric mirror charge effect, enhancing the overall SERS activity.

lar Au nanodisks with a diameter of 51 ± 8 nm (Fig. 2B) *via* a tip-selective etching process using $AuCl_4^-$ ions as the etchant, as described in previous literature.[8] Subsequently, in a cetyltri-methylammonium bromide (CTAB) environment, $AuCl_4^-$ ions were further reduced along the edges of the nanodisks, yielding Au h-NPLs with a diameter of 133 ± 9 nm and newly developed side facets (Fig. 2C). The resulting h-NPLs exhibit basal planes consisting of {111} facets on the top and bottom, with twelve edge sides alternating between {111} and {100} facets,[28] resulting in the formation of a total of 14 facets (Fig. 2E). To deposit Ag onto the Au h-NPLs, we introduced cetyltrimethyl-ammonium chloride (CTAC) as the capping agent, $AgNO_3$ as the metal precursor, ascorbic acid as the reducing agent, and NaOH as the pH controller. Notably, the resulting Au@Ag h-NPLs retained their hexagonal shape with sharp side edges, indicating that Ag growth occurred epitaxially without forming an Au–Ag atomic alloy (Fig. 2D). CTAC was specifically chosen to passivate side growth and facilitate epitaxial deposition. As a cationic surfactant with a simple structure, CTAC forms strong electrostatic interactions with Ag ions, enabling their adsorption onto the Au NPL surface, which facilitates rapid reduction and subsequent NP growth (Fig. 2F). This selective epitaxial growth of Ag on Au h-NPLs allows for an in-depth investigation of the effects of hot spot density when assembled

into columnar SPs, a topic discussed later. The successful uniform epitaxial growth of Ag was confirmed through energy-dispersive X-ray spectroscopy (EDS) mapping and transmission electron microscopy (TEM) images, which distinguish Au and Ag by color (red for Au and green for Ag) in both Au h-NPLs and Au@Ag h-NPLs (Fig. 2G and H). In addition to Ag growth on the top and bottom Au planes, six protruding Ag domains were observed, extending from the (111) side facets, with less Ag deposited on the (100) facets. This led to asymmetric Au@Ag h-NPLs, a result of the unique crystal structure of the core Au h-NPLs, which exhibit alternating (111) and (100) facets with differing Ag growth kinetics. The schematic in Fig. 2F illustrates this asymmetric Ag growth pattern. This unique growth pattern yields flat and sharp Ag edges critical for near-field collection while maintaining the structural integrity of the NPLs (refer to Fig. S1† for additional STEM images highlighting the side facets of asymmetric Ag growth).

We examined the UV-vis-NIR spectra during the morphological evolution from Au triangular nanodisks to Au circular nanodisks, Au h-NPLs, and finally Au@Ag h-NPLs (Fig. 2I). Anisotropic NPLs typically exhibit two distinct plasmonic modes: in-plane and out-of-plane dipole modes,[8] similar to those observed in elongated nanorod systems.[29] Initially, the in-plane quadrupole mode of Au triangular nanodisks at λ =
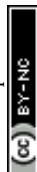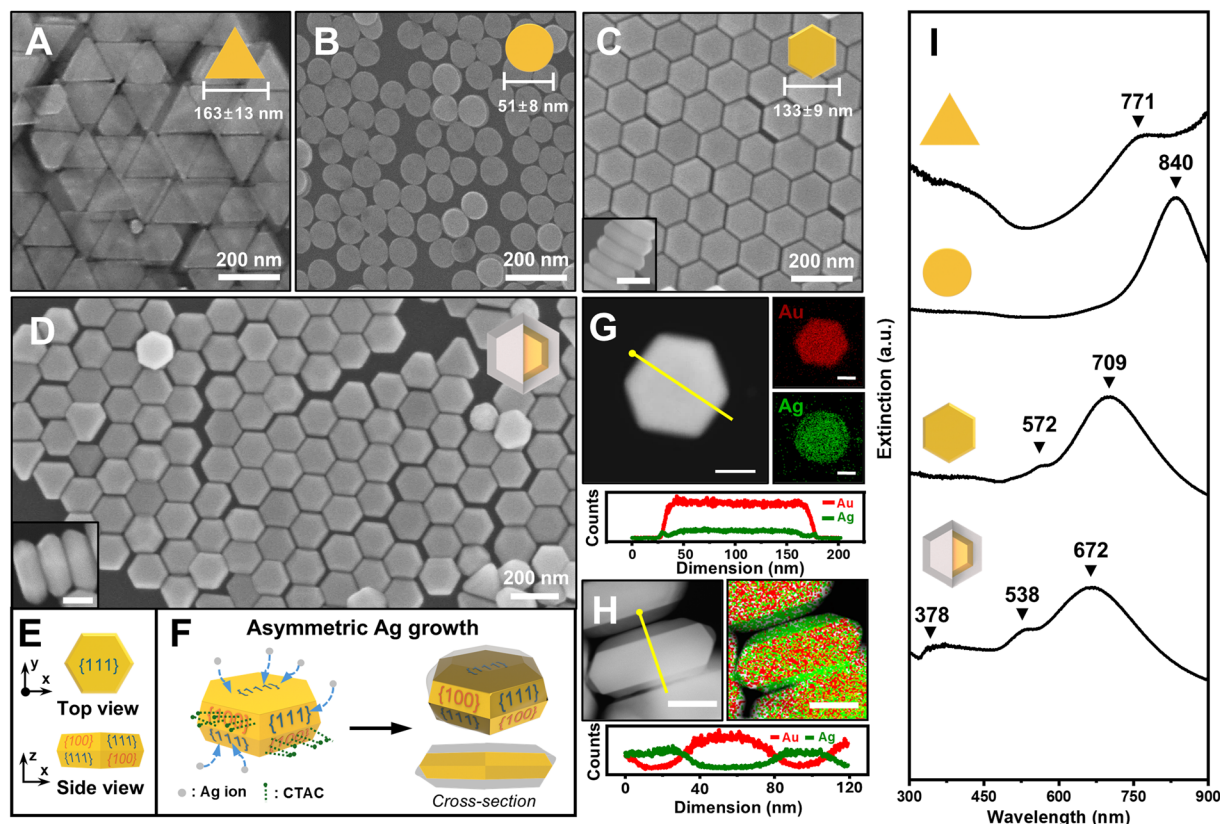
Fig. 2 Morphological and optical characterization of Au and Au@Ag h-NPLs. FE–SEM images of (A) Au triangular NPLs, (B) Au circular NPLs, (C) Au h-NPLs, and (D) Au@Ag h-NPLs. Scale bars in the insets of (C) and (D) are 100 nm. (E) Schematic representation of the crystallographic facets of Au h-NPLs, featuring two {111} top and bottom planes and alternating twelve side facets of {111} and {100} planes. (F) Cartoon illustrating asymmetric Ag shell growth on Au h-NPLs. EDS mapping images and line spectra scanned along the (G) horizontal and (H) vertical planes of Au@Ag h-NPLs. (I) UV-vis-NIR spectra corresponding to panels A–D.

771 nm shifted sequentially to 840 nm and then to 709 nm after the tip-selective etching and overgrowth of Au h-NPLs, respectively. The appearance of an out-of-plane mode at 572 nm in the Au h-NPLs indicated sufficient side thickness, in contrast to the Au circular nanodisks, which lacked an out-of-plane mode due to their very thin structure. Following the deposition of Ag onto the Au h-NPLs, both the in-plane and out-of-plane modes blueshifted to 672 nm and 538 nm, respectively, due to the decrease in aspect ratio (defined as diameter D, over thickness, L). Additionally, the LSP peak at 378 nm confirmed the successful deposition of Ag, as this wavelength is characteristic of intrinsic Ag properties.[17]

Fabrication of ready-to-use and free-standing SPs of Au@Ag h-NPLs

We fabricated ready-to-use, free-standing columnar SPs using an upside-down drying method. The resulting SPs, composed of h-NPLs, formed micron-sized, pillar-like supercrystals with face-to-face alignment, exposing nanogaps perpendicular to the incoming laser to maximize near-field enhancement.[20] Briefly, the colloidal solution was drop-cast onto a Si wafer substrate, and the upside-down drying method was employed by attaching the backside of the substrate to a Teflon cell.

This cell was placed in a chamber maintaining high and constant pressure (*i.e.*, ensuring a slow evaporation rate), allowing the samples to dry over 12 h. The formation of these SPs is influenced by the depletion force, which depends on the concentration of surfactants like CTAC in the solution. CTAC forms micelles in solution, and the concentration of these micelles is lower near the particles than in other regions of the solution. This gradient creates a region of lower osmotic pressure around the particles, resulting in an imbalance that facilitates depletion forces between them. To determine the optimal concentration for SP formation, we varied the CTAC concentration from 0, 0.1, 1.0, 2.0, 5.0, 10, to 100 mM during the upside-down drying process (Fig. 3A–D; see Fig. S2† for results with 0.1, 1.0, and 5.0 mM CTAC). In the absence of CTAC (Fig. 3A), randomly oriented aggregates were observed. At a CTAC concentration of 0.1 mM (Fig. S2A†), face-to-face alignment began to appear, but the attractive forces between particles were insufficient to form distinct, micron-sized supercrystals. At 1 mM CTAC (Fig. S2B†), parallel string arrays began to form, enabling particles to behave as individual aggregates. Increasing the CTAC concentration to 2 mM produced the optimal micelle concentration for elongated columnar SPs
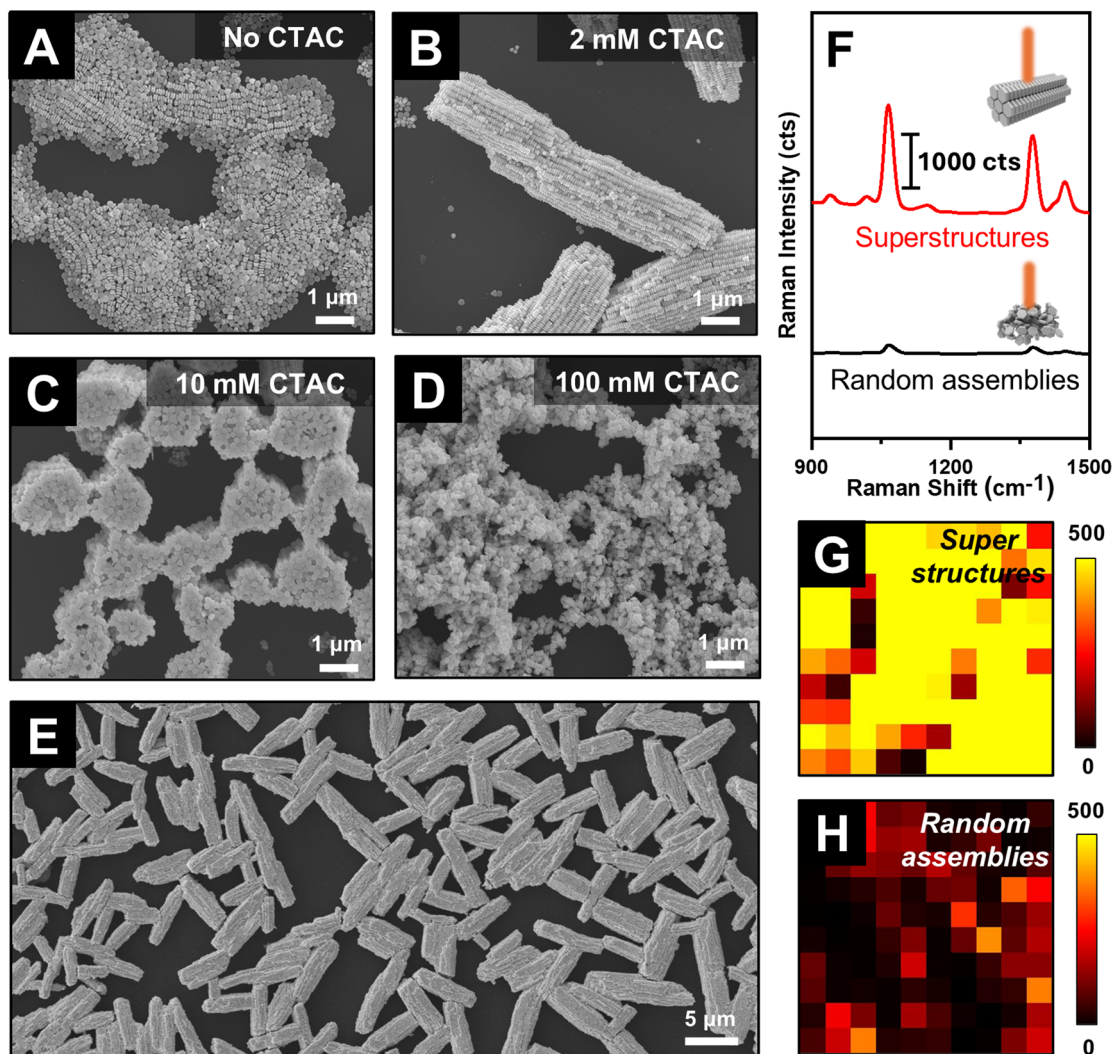
Fig. 3 (A–D) FE-SEM images of assemblies formed under different CTAC concentrations: 0, 2, 10, and 100 mM. (E) Large-scale FE-SEM image of ordered columnar SPs composed of Au@Ag h-NPLs. (F) SERS spectra of 2-NTT (10^{-2} M) obtained from SPs and randomly assembled Au@Ag h-NPLs under 785 nm excitation. (G and H) Raman signal mapping images corresponding to panel F, where each pixel represents 5 μm.

with uniform size distribution (Fig. 3B). These SPs exhibited micron-sized dimensions and elongated superstructures, causing them to lie flat on the substrate with face-to-face nanogaps oriented upwards (see Fig. S3† for the estimation of the number of particles in a single SP chunk). At a CTAC concentration of 10 mM (Fig. 3C), very short SPs formed, standing upright rather than lying flat, and began to lose their packing order. At 100 mM CTAC (Fig. 3D), the SPs lost their organized structure entirely, resulting in a random assembly. This behavior indicates that moderate CTAC concentrations promote organized assembly, while excessive CTAC concentrations disrupt the interactions necessary for coherent superstructure growth, leading to disordered arrangements. A low-magnification FE-SEM image of SPs formed at a CTAC concentration of 2 mM (Fig. 3E) revealed uniformly sized, well-distributed, and well-defined SPs. This

ordered assembly is critical, as it ensures the laser beam aligns perpendicularly to the columnar structures, enabling more efficient excitation of plasmonic modes and stronger enhancement in magnitude. Furthermore, the continuous sequence of nanogaps in the ordered assembly increases gap density, which enhances near-field focusing. The dense nanogap distribution facilitates stronger localization of the electromagnetic field, significantly improving performance in SERS, as discussed further below.

Notably, significantly higher Raman signals for 2-naphthalenethiol (2-NTT) were observed in the SPs (red spectrum in Fig. 3F) compared to those in the random assembly (black spectrum in Fig. 3F). This SERS effect is clearly demonstrated in the SERS mapping images (Fig. 3G and H), where the SPs exhibit much stronger and more uniform signal distributions than the random assembly. These results confirm the critical

role of face-to-face nanogaps oriented perpendicular to the incoming laser and the high density of hot spots in enhancing SERS and generating uniform signals.

Effect of Ag shell on SERS enhancement

To elucidate the effects of Ag shell thickness on SERS measurements, three samples of Au@Ag h-NPLs with varying Ag thicknesses were prepared. As shown in Fig. 4A–C, the Ag shell thickness was tunable to 4.5 nm, 6.5 nm, and 9.5 nm by adjusting the concentrations of $AgNO_3$ added during growth, while the lateral dimensions of the Ag remained relatively consistent (see Fig. S4† for the size histogram of Ag thickness). The size data and TEM images indicate that the growth occurred predominantly along the z-axis of the Au h-NPLs (i.e., epitaxial growth perpendicular to the basal planes), with minimal lateral growth, likely due to the presence of (111) side facets. The increase in Ag thickness was further confirmed by UV-vis-NIR spectroscopy, which showed a consistent blueshift of the in-plane dipole mode from 686 nm to 672 nm to 663 nm as the Ag thickness increased from 4.5 nm to 6.5 nm to 9.5 nm (Fig. S5†).

Additionally, the characteristic Ag peak around 400 nm exhibited consistent intensity increases with increasing Ag thickness, clearly indicating controllable Ag growth. The epi-

taxial and uniform growth of Ag on Au without altering the shape facilitated the formation of columnar SPs under similar experimental conditions. This process is confirmed by Fig. 4A–C, with panels 1 to 4 showing the building blocks, parallel string array superstructures, and columnar SPs at different magnifications. However, when the Ag layer exceeded a thickness of 9.5 nm, the overall morphology was compromised, resulting in the formation of randomly oriented aggregates (Fig. S6†).

From a SERS perspective, we hypothesized that increasing the thickness of the Ag layer would reduce the density of hot spots within the resulting SPs under the laser spot, leading to a decline in signal intensity. Contrary to this expectation, the observed trend revealed that the SERS signal intensity increased as the Ag shell thickness grew. The SERS spectra obtained from four types of SPs—pure Au h-NPLs and Au@Ag h-NPLs with Ag thicknesses of 4.5, 6.5, and 9.5 nm (denoted as $Au@Ag_{4.5}$, $Au@Ag_{6.5}$, and $Au@Ag_{9.5}$, respectively)—showed a clear increase in Raman intensity at 1065 cm^{-1} for 2-NTT, from 472 cts, 1043 cts, and 1795 cts to 2657 cts (Fig. 4D and E; see Fig. S8 to S10† for individual SERS measurements). The relative standard deviation (RSD) values for each condition in Fig. 4E were quantified as 31.6%, 16.1%, 3.3%, and 19.5%, respectively, indicating not only a rising trend in intensity but
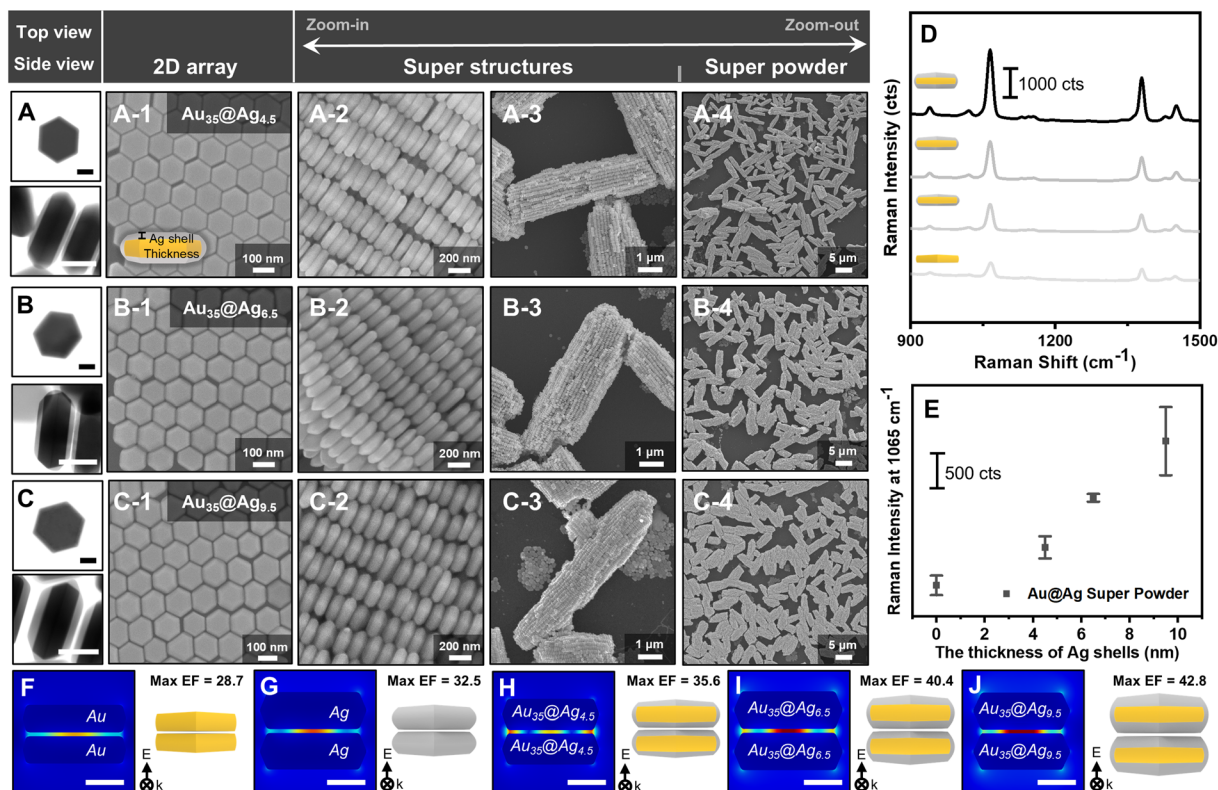
Fig. 4 TEM and FE-SEM images of SPs composed of $Au_{35}@Ag_t$ h-NPLs with varying shell thicknesses: (A) $Au_{35}@Ag_{4.5}$ h-NPLs, (B) $Au_{35}@Ag_{6.5}$ h-NPLs, and (C) $Au_{35}@Ag_{9.5}$ h-NPLs. (D) SERS spectra of 2-NTT (10^{-2} M) measured on SPs formed from $Au_{35}@Ag_t$ h-NPLs; the black spectrum corresponds to $Au_{35}@Ag_{9.5}$ h-NPLs, showing the highest intensity. (E) Raman peak intensity at 1065 cm^{-1} for 2-NTT increases with Ag shell thickness. (F–J) Schematic illustrations and near-field distribution images of various dimeric configurations. The Raman intensity at 1065 cm^{-1} is averaged from three independent measurements. Scale bars denote 50 nm.

also reasonable signal consistency across measurements (Fig. S7†). Finite element method (FEM) simulations for dimeric configurations further demonstrated that all investigated Au@Ag h-NPL samples exhibited higher enhancement factors (EFs; Fig. 4H–J) compared to their pure component counterparts (e.g., pure Au–Au or pure Ag–Ag dimers, shown in Fig. 4F and G).

This finding underscores the role of the core–shell structure in enhancing the near-field effects.

In terms of intra-particle plasmonic coupling (i.e., within a single entity), the enhancement of the SERS signal is attributed to interactions at the interface between the Ag shell and the Au core. As the Ag shell grows thicker, the influence of the Au core diminishes, while the plasmonic characteristics of the Ag shell become more pronounced, resembling those of pure Ag NPs. Given that SERS is dominated by the properties of the top surface layer, an Ag shell thickness of approximately 9.5 nm allows the structure to behave as a pure Ag surface, thereby maximizing SERS signal enhancement.

In terms of near-field collection within the face nanogaps formed in the dimers, the stronger electromagnetic field enhancement observed in the Au core–Ag shell dimers (Fig. 4H–J) compared to pure Ag h-NPLs (Fig. 4G) can be attributed to the synergistic effects of (1) electron mobility between the metals and (2) electronic ligand interactions. In this bimetallic core–shell nanostructure, the higher electronegativity of Au relative to Ag drives electron transfer from Ag to Au, known as electron compensation, resulting in a redistribution of electron density through backdonation from Au to Ag and correcting the electron balance between Au and Ag.[30] This migration induces plasmonic coupling between the core and shell, optimizing the LSPR frequency for enhanced electromagnetic effects at the interfaces between Au and Ag. The redistribution of electrons also modifies the surface charge of the Ag shell, leading to more efficient plasmon resonance under incident light. This behavior enables the Au core–Ag shell structure to sustain higher plasmonic intensities compared to pure Ag. Consequently, under identical laser intensities, the enhanced electromagnetic field produces stronger Raman scattering, providing superior sensitivity.

Another key factor contributing to the enhanced SERS sensitivity is the electronic ligand effect.[31,32] The presence of Au in the core influences the electronic structure of the Ag shell, slightly reducing the electron density on the Ag surface. This reduction increases the chemical reactivity of the Ag shell, facilitating stronger interactions between the metal surface and the target molecules. These enhanced chemical interactions enable the Au core–Ag shell structure to more efficiently adsorb analyte molecules. This aspect is critical for SERS performance, as the Raman signal intensity depends strongly on the proximity and binding strength of the molecules to the metallic surface. Thus, the synergistic interplay between the electronic ligand effect and plasmonic enhancement ensures that the structure delivers not only high sensitivity but also high selectivity for various molecular species.

Mirror charge effect through the heterogeneous interface between pure Au and Au@Ag h-NPLs

To maximize near-field collection through nanoalloying, Au@Ag NPLs were mixed with pure Au h-NPLs to increase heterogeneous interfaces via inter- and intra-particle plasmonic coupling. This strategy leverages intra-particle plasmonic coupling—stemming from electron mobility and the electronic ligand effect at the bimetallic Au–Ag interfaces within individual Au@Ag h-NPLs—and inter-particle plasmonic coupling, also known as the "mirror charge effect". In this system, nanogaps formed within the heterogeneous building blocks of Au and Ag facilitate effective polarization due to the differing electron affinities of Au and Ag, leading to enhanced near-field collection. In assemblies of Au h-NPLs and Au core–Ag shell NPLs with volumetric ratios of 75/25, 50/50, 25/75, and 0/100 and varying Ag shell thicknesses ($Ag_{4.5}$ (Fig. 5A–D), $Ag_{6.5}$ (Fig. 5E–H), and $Ag_{9.5}$ (Fig. 5I–L)), the resulting superstructures remained highly ordered. EDS mapping images and atomic ratios of Au and Ag confirmed that the Au–Ag binary columnar SPs contained both elements. The increasing atomic percentage of Ag was identifiable through the gradual increase in Ag color contrast, verifying the successful creation of controllable "nanoalloy" structures (see Fig. S11 and S12† for additional FE-SEM images of binary SPs with different proportions of Au and Ag, and pure Au h-NPLs, respectively).

All nanoalloyed SPs, regardless of Ag shell thickness, exhibited higher SERS intensities compared to SPs composed of pure Au or Au@Ag h-NPLs alone, primarily due to the increased probability of bimetallic interparticle coupling in the assemblies (Fig. 6A–D; see Fig. S13–S15† for raw SERS data and Fig. S16† for the RSD values). When the SPs contained a high proportion of Au h-NPLs, the lower plasmonic quality factor of the Au SPs did not significantly contribute to the SERS effect. However, as the proportion of Au@Ag h-NPLs increased to 75% by volume, the SERS signals rose substantially due to the enhanced mirror charge effect, achieving a signal ten times higher than that of SPs composed entirely of Au@Ag h-NPLs. This finding highlights the critical role of mirror charge effects in heterogeneous nanogaps for enhanced SERS performance. Mathematically, a 1 : 1 ratio of Au to Au@Ag h-NPLs would generate the highest number of heterogeneous interfaces. However, it should be noted that the assembly is not formed through a perfectly alternating one-to-one sequence. Moreover, it is currently challenging to precisely determine the sequence of assembly, as Au@Ag h-NPLs also exhibit Au signals in EDS mapping, making it difficult to accurately quantify each component within the superstructures. For this reason, we varied the volumetric ratio of each building block to experimentally identify the optimized composition that yields the strongest near-field focusing effect. Based on our current experimental assembly process, an Au/Au@Ag ratio of 25/75 was found to provide the strongest SERS enhancement, suggesting that this composition yields the highest prevalence of heterogeneous interfaces.
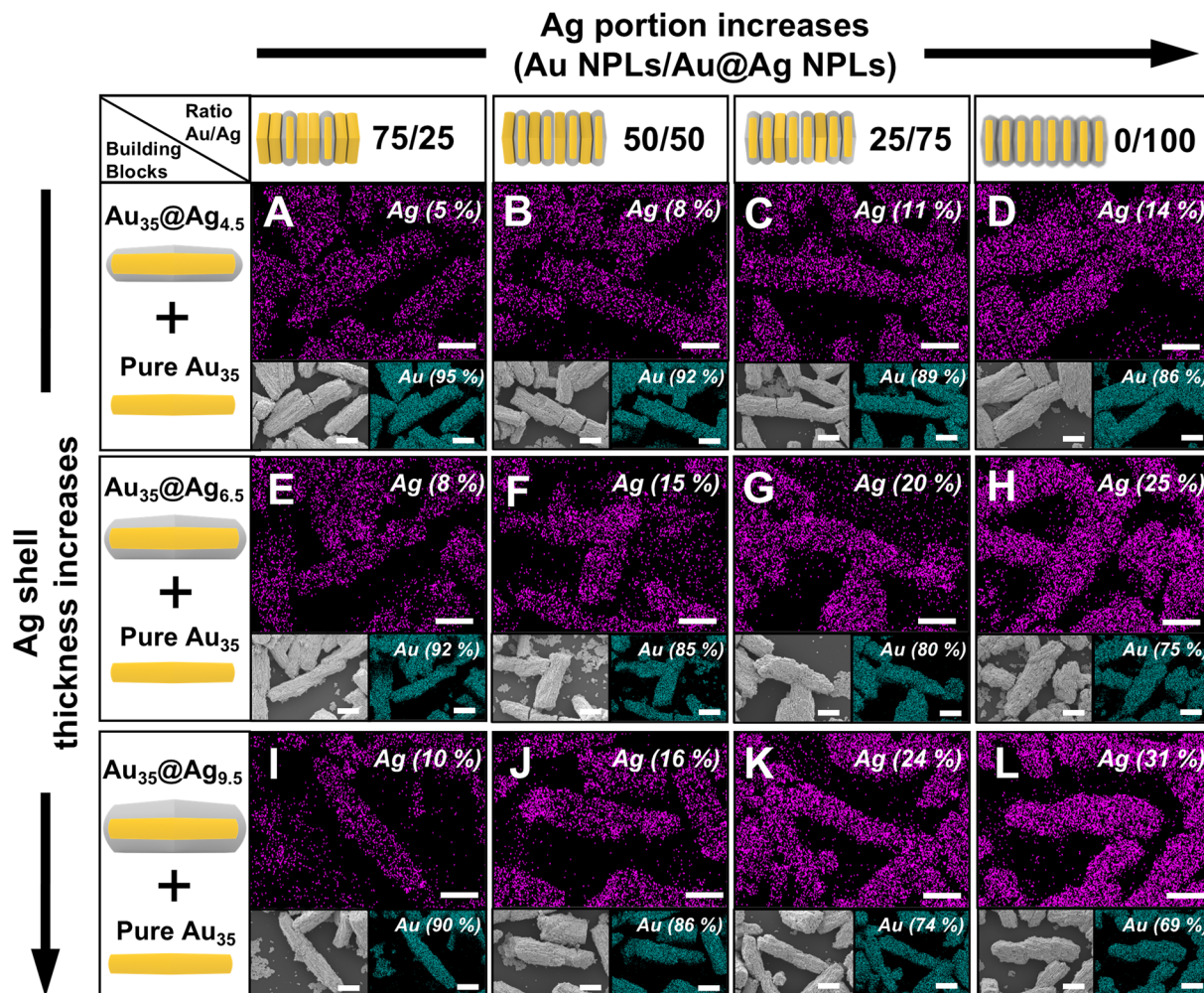
Fig. 5 FE–SEM and EDS mapping images of varying ratios of Au h-NPLs. (A–D) $Au_{35}@Ag_{4.5}$ (Au/Ag): 75/25, 50/50, 25/75 and 0/100, (E–H) $Au_{35}@Ag_{6.5}$ (Au/Ag): 75/25, 50/50, 25/75, 0/100 and (I–L) $Au_{35}@Ag_{9.5}$ (Au/Ag): 75/25, 50/50, 25/75, 0/100. All scale bars denote 2 μm.

These results were further validated using FEM simulations on dimers. As shown in Fig. 6E–G, near-field enhancement was strongest when Au and $Au@Ag_{6.5}$ h-NPLs were aligned, achieving an EF of 69.4, surpassing that of pure Au dimers, pure Ag dimers, or Au@Ag h-NPL dimers. When the Ag shell thickness exceeded a critical threshold ($Au@Ag_{9.5}$ h-NPL, Fig. 6G), the combined effects of inter-mirror charges between Au h-NPLs and the Ag shell, as well as intra-mirror charges within the Au core-Ag shell NPL, became less pronounced. Conversely, when the Ag shell thickness was below this threshold ($Au@Ag_{4.5}$ h-NPL, Fig. 6E), the bimetallic characteristics of Au and Ag were less dominant, hindering the effective formation of mirror charge effects. These observations align with the near-field distribution of dimers shown in Fig. 6E and G. Fig. 6D illustrates SERS signal comparisons for SPs with various configurations. Notably, while the SERS signal intensity increased with thicker Ag shells in superstructures composed solely of Au@Ag h-NPLs, this trend reversed upon introducing Au h-NPLs into the mixture. $Au@Ag_{6.5}$ h-NPLs, with an intermediate Ag shell thickness, demonstrated the strongest

electromagnetic field enhancement. Thus, the relative proportion of bimetallic building blocks and an optimal Ag shell thickness are both crucial for maximizing the enhancement derived from inter- and intra-interface charge interactions. To avoid interactions between individual supercrystals and to examine these findings in greater detail, we isolated single chunks of Au@Ag h-NPLs with varying Ag proportions and conducted SERS mapping (Fig. S17†). Consistent with the results in Fig. 6A–D, mixing binary building blocks and increasing the proportion of Au@Ag h-NPLs relative to pure Au h-NPLs enhanced SERS intensities.

Nanoalloying of binary SPs for practical SERS substrates toward detection of pesticides

One of the key applications where SP-type SERS substrates offer significant advantages is the on-site detection of toxic chemicals, such as pesticides, for food safety and the identification of unknown molecules, including chemical warfare agents.[6,33] The SPs described in this paper are free-standing, ready-to-use, and capable of being stored in any container,
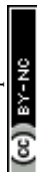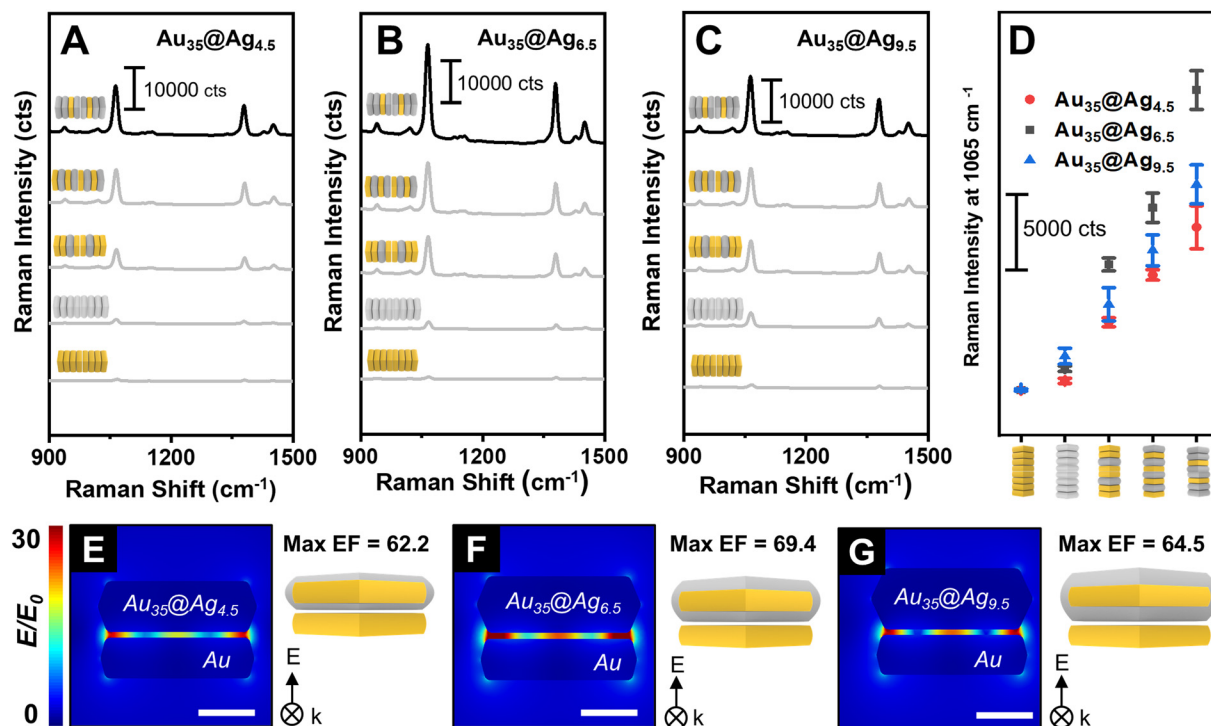
Fig. 6 (A–C) SERS spectra of SPs composed of $Au_{35}@Ag_t$ h-NPLs with varying Ag shell thicknesses as well as relative volumetric ratios of Au h-NPLs and Au@Ag h-NPLs. The black spectra in panels A–C correspond to the superstructure of h-NPLs with an Au : Au@Ag ratio of 1 : 3, which exhibits the highest signal intensity. (D) Plot of SERS peak intensities at 1065 cm^{-1} for different shell thicknesses in Au–Ag mixtures: $Au_{35}@Ag_{4.5}$ (red trace), $Au_{35}@Ag_{6.5}$ (black trace), and Ag-$Au_{35}@Ag_{9.5}$ (blue trace) with varying ratios of Au and Au@Ag h-NPLs. (E–G) FEM simulations showing electric field enhancement for dimers consisting of an Au h-NPL paired with (E) $Au_{35}@Ag_{4.5}$, (F) $Au_{35}@Ag_{6.5}$, and (G) $Au_{35}@Ag_{9.5}$ h-NPLs. Scale bars denote 50 nm.

enabling easy handling and on-demand, on-site detection. To validate the practical application of h-NPL-based SPs in SERS, we performed SERS-based detection of thiram, a common pesticide component (Fig. 7A–C). In this experiment, the surface of an apple peel was contaminated with thiram, and SPs dried

on a translucent optical patch were attached for 5 min before being peeled off for SERS measurement. SERS spectra were recorded at varying thiram concentrations. Under identical conditions at a thiram concentration of 10^{-2} M, the heterogeneous columnar SPs with a 1 : 3 Au-to-Ag ratio (Fig. 7F)
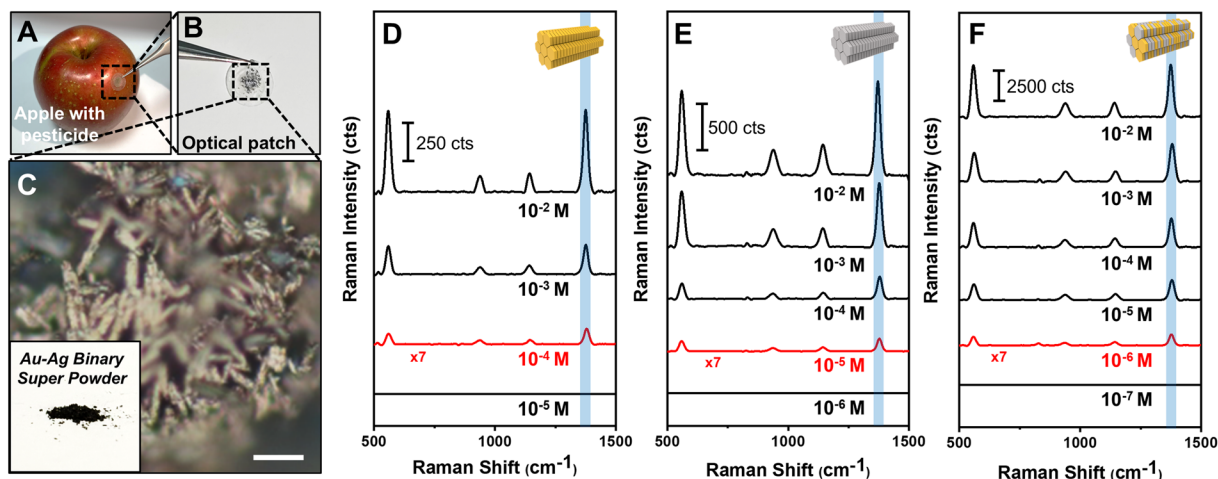
Fig. 7 (A–C) Optical photographs of SPs attached to apple peel for SERS-based detection of thiram. The scale bar in panel C represents 10 μm. SERS spectra of thiram at varying concentrations using (D) Au h-NPL SPs, (E) Au@Ag h-NPL SPs, and (F) heterogeneous Au–Ag h-NPL SPs.

demonstrated signal intensities (3809 cts) that were six and four times higher than those of single-component pure Au SPs (598 cts) (Fig. 7D) and Au@Ag h-NPLs (1101 cts) (Fig. 7E), respectively. Furthermore, the binary SPs exhibited a lower limit of detection (LOD) of 10^{-6} M compared to 10^{-4} M and 10^{-5} M for pure Au SPs and Au@Ag h-NPL SPs, respectively (indicated by red lines in the data; see Fig. S18† for calibration curves). Notably, FE-SEM images taken after thiram detection confirmed that the overall structural integrity of the SPs remained well preserved, highlighting their robustness and stability for repeated or prolonged use (Fig. S19†). This enhanced SERS performance is attributed to the synergistic effects of the bimetallic properties within individual particles and the mirror-charge interactions between particles. These bimetallic nanoalloyed SPs hold great promise for portable and immediate on-site detection applications.

Conclusions

In this study, we demonstrated the synthesis, assembly behavior, and plasmonic properties of Au core–Ag shell h-NPLs and their heterogeneous interactions when mixed with pure Au h-NPLs. By precisely manipulating the surface energy differences of the core Au h-NPLs, which exhibit twelve alternating crystalline side facets, epitaxial and asymmetric Ag growth with tunable shell thicknesses were achieved. Using these engineered NPs, we successfully fabricated free-standing, ready-to-use columnar SPs composed of parallel "wire-like string" arrays via an upside-down assembly method. This approach ensures that the face-to-face nanogaps between individual h-NPLs are aligned perpendicular to incoming light, maximizing the density of hot spots. Our findings revealed that the core–shell structure is crucial for enhancing SERS performance, with the Ag shell thickness playing a pivotal role. Optimizing the interactions at intra- and inter-interfaces within the nanostructures led to improved near-field focus. This enhancement was most pronounced in binary nanoalloys fabricated from a mixture of Au@Ag h-NPLs and pure Au h-NPLs. The observed nanoalloying effect was attributed to the synergistic contributions of bimetallic interactions within the Au core–Ag shell structure (intra-interface) and the mirror charge effect between neighboring NPLs (inter-particle). Through a combination of experimental SERS measurements and theoretical validation via FEM simulations of dimeric configurations, we demonstrated the importance of interfacial engineering in Au–Ag core–shell NPLs. The nanomixing of binary components significantly enhanced near-field and far-field electromagnetic field factors. Moreover, the ability to fine-tune shell thickness and assembly structure, alongside the formation of columnar SPs, opens new avenues for optimizing SERS performance, particularly for on-site detection of toxic chemicals. These findings provide valuable insights into the design of highly efficient plasmonic NPs, with promising potential for applications in chemical sensing and biodetection.

Author contributions

The manuscript was written through contributions of all authors. All authors have given approval to the final version of the manuscript.

Data availability

The data supporting this article have been included as part of the ESI.†

Conflicts of interest

There are no conflicts to declare.

Acknowledgements

References

1 C. Gong and M. S. Leite, Noble Metal Alloys for Plasmonics, *ACS Photonics*, 2016, **3**(4), 507–513.
2 C. Gong, M. R. S. Dias, G. C. Wessler, J. A. Taillon, L. G. Salamanca-Riba and M. S. Leite, Near-Field Optical Properties of Fully Alloyed Noble Metal Nanoparticles, *Adv. Opt. Mater.*, 2017, **5**(1), 1600568.
3 S. Liu, G. Y. Chen, P. N. Prasad and M. T. Swihart, Synthesis of Monodisperse Au, Ag, and Au-Ag Alloy Nanoparticles with Tunable Size and Surface Plasmon Resonance Frequency, *Chem. Mater.*, 2011, **23**(18), 4098–4101.
4 T. Shibata, B. A. Bunker, Z. Y. Zhang, D. Meisel, C. F. Vardeman and J. D. Gezelter, Size-dependent spontaneous alloying of Au-Ag nanoparticles, *J. Am. Chem. Soc.*, 2002, **124**(40), 11989–11996.
5 V. Puravankara, A. Manjeri, Y. H. Kim, Y. Kitahama, K. Goda, P. K. Dwivedi and S. D. George, Surface-Enhanced Raman spectroscopy for Point-of-Care Bioanalysis: From lab to field, *Chem. Eng. J.*, 2024, **498**, 155163.
6 T. Wang, S. P. Wang, Z. H. Cheng, J. C. Wei, L. L. Yang, Z. F. Zhong, H. Hu, Y. T. Wang, B. P. Zhou and P. Li, Emerging core-shell nanostructures for surface-enhanced

Raman scattering (SERS) detection of pesticide residues, *Chem. Eng. J.*, 2021, **424**, 130323.

7 J. E. Millstone, S. Park, K. L. Shuford, L. D. Qin, G. C. Schatz and C. A. Mirkin, Observation of a quadrupole plasmon mode for a colloidal solution of gold nanoprisms, *J. Am. Chem. Soc.*, 2005, **127**(15), 5312–5313.

8 S. Hong, K. L. Shuford and S. Park, Shape Transformation of Gold Nanoplates and their Surface Plasmon Characterization: Triangular to Hexagonal Nanoplates, *Chem. Mater.*, 2011, **23**(8), 2011–2013.

9 L. Chen, F. Ji, Y. Xu, L. He, Y. F. Mi, F. Bao, B. Q. Sun, X. H. Zhang and Q. Zhang, High-Yield Seedless Synthesis of Triangular Gold Nanoplates through Oxidative Etching, *Nano Lett.*, 2014, **14**(12), 7201–7206.

10 J. Kim, S. W. Lee, J. Son, J. Kim, H. Hilal, M. Park, I. S. Jung, J. M. Nam and S. Park, Plasmonic Cyclic Au Nanosphere Hexamers, *Small*, 2023, **19**(7), 2205956.

11 B. K. Choi, J. Kim, Z. Luo, J. Kim, J. H. Kim, T. Hyeon, S. Mehraeen, S. Park and J. Park, Shape Transformation Mechanism of Gold Nanoplates, *ACS Nano*, 2023, **17**(3), 2007–2018.

12 S. Yoo, J. Lee, J. Kim, J. M. Kim, M. Haddadnezhad, S. Lee, S. Choi, D. Park, J. M. Nam and S. Park, Silver Double Nanorings with Circular Hot Zone, *J. Am. Chem. Soc.*, 2020, **142**(28), 12341–12348.

13 S. Lee, S. Kwon, S. Lee, M. J. Oh, I. Jung and S. Park, Combinatorial Effect of Tricomponent Dual-Rim Nanoring Building Blocks: Label-Free SERS Detection of Biomolecules, *Nano Lett.*, 2024, **24**(13), 3930–3936.

14 Y. R. Wu, X. J. Sun, Y. Yang, J. M. Li, Y. Zhang and D. Qin, Enriching Silver Nanocrystals with a Second Noble Metal, *Acc. Chem. Res.*, 2017, **50**(7), 1774–1784.

15 Y. Bae, N. H. Kim, M. Kim, K. Y. Lee and S. W. Han, Anisotropic assembly of Ag nanoprisms, *J. Am. Chem. Soc.*, 2008, **130**(16), 5432–5433.

16 C. Xue, G. S. Métraux, J. E. Millstone and C. A. Mirkin, Mechanistic study of photomediated triangular silver nanoprism growth, *J. Am. Chem. Soc.*, 2008, **130**(26), 8337–8344.

17 Q. Zhang, N. Li, J. Goebl, Z. D. Lu and Y. D. Yin, A Systematic Study of the Synthesis of Silver Nanoplates: Is Citrate a "Magic" Reagent?, *J. Am. Chem. Soc.*, 2011, **133**(46), 18931–18939.

18 G. P. Lee, Y. C. Shi, E. Lavoie, T. Daeneke, P. Reineck, U. B. Cappel, D. M. Huang and U. Bach, Light-Driven Transformation Processes of Anisotropic Silver Nanoparticles, *ACS Nano*, 2013, **7**(7), 5911–5921.

19 S. Lee, Q. Zhao, S. Lee, I. Choi, S. Lee, I. Jung and S. Park, Two- and Three-Dimensional Ag-Au Nanoalloying: Heterogeneous Building Blocks Enhancing Near-Field Focusing, *ACS Nano*, 2024, **18**(43), 29880–29890.

20 M. Haddadnezhad, I. S. Jung, M. J. Oh and S. Park, Ready-to-Use Free-Standing Super-Powder Made with Complex Nanoparticles for SERS, *Adv. Mater.*, 2024, **36**(26), 2400068.

21 J. F. Li, Y. J. Zhang, S. Y. Ding, R. Panneerselvam and Z. Q. Tian, Core-Shell Nanoparticle-Enhanced Raman Spectroscopy, *Chem. Rev.*, 2017, **117**(7), 5002–5069.

22 F. Novotny, J. Plutnar and M. Pumera, Plasmonic Self-Propelled Nanomotors for Explosives Detection via Solution-Based Surface Enhanced Raman Scattering, *Adv. Funct. Mater.*, 2019, **29**(33), 1903041.

23 D. Chahinez, T. Reji and R. Andreas, Modeling of the surface plasmon resonance tunability of silver/gold core-shell nanostructures, *RSC Adv.*, 2018, **8**(35), 19616–19626.

24 K. D. Osberg, M. Rycenga, N. Harris, A. L. Schmucker, M. R. Langille, G. C. Schatz and C. A. Mirkin, Dispersible Gold Nanorod Dimers with Sub-5 nm Gaps as Local Amplifiers for Surface-Enhanced Raman Scattering, *Nano Lett.*, 2012, **12**(7), 3828–3832.

25 L. D. Qin, S. L. Zou, C. Xue, A. Atkinson, G. C. Schatz and C. A. Mirkin, Designing, fabricating, and imaging Raman hot spots, *Proc. Natl. Acad. Sci. U. S. A.*, 2006, **103**(36), 13300–13303.

26 C. Xue, J. E. Millstone, S. Y. Li and C. A. Mirkin, Plasmon-driven synthesis of triangular core-shell nanoprisms from gold seeds, *Angew. Chem., Int. Ed.*, 2007, **46**(44), 8436–8439.

27 K. Park, L. F. Drummy and R. A. Vaia, Ag shell morphology on Au nanorod core: role of Ag precursor complex, *J. Mater. Chem.*, 2011, **21**(39), 15608–15618.

28 J. Kim, I. Jung, M. J. Oh, H. Hilal, W. Park and S. Park, Shape Evolution of Two-Dimensional Au Hexagonal Nanoplates into Pseudo Three-Dimensional Oblate Spheroids, *Chem. Mater.*, 2023, **35**(10), 3976–3984.

29 I. Jung, M. Kim, M. Kwak, G. Kim, M. Jang, S. M. Kim, D. J. Park and S. Park, Surface plasmon resonance extension through two-block metal-conducting polymer nanorods, *Nat. Commun.*, 2018, **9**, 8302.

30 Y. L. Feng, G. R. Wang, Y. Chang, Y. Cheng, B. B. Sun, L. M. Wang, C. Y. Chen and H. Y. Zhang, Electron Compensation Effect Suppressed Silver Ion Release and Contributed Safety of Au@Ag Core-Shell Nanoparticles, *Nano Lett.*, 2019, **19**(7), 4478–4489.

31 S. Pande, S. K. Ghosh, S. Praharaj, S. Panigrahi, S. Basu, S. Jana, A. Pal, T. Tsukuda and T. Pal, Synthesis of normal and inverted gold-silver core-shell architectures in β-cyclodextrin and their applications in SERS, *J. Phys. Chem. C*, 2007, **111**(29), 10806–10813.

32 W. J. Tang and G. Henkelman, Charge redistribution in core-shell nanoparticles to promote oxygen reduction, *J. Chem. Phys.*, 2009, **130**(19), 194504.

33 M. J. Oh, S. Kwon, S. Lee, I. Jung and S. Park, Octahedron in a Cubic Nanoframe: Strong Near-Field Focusing and Surface-Enhanced Raman Scattering, *ACS Nano*, 2024, **18**(10), 7656–7665.